Analysis of Interannual Changes in Northern Vegetation Activity Observed in AVHRR Data From 1981 to 1994

Nikolay V. Shabanov, Liming Zhou, Yuri Knyazikhin, Ranga B. Myneni, and Compton J. Tucker

Abstract—This paper reports on the analysis of Pathfinder AVHRR land (PAL) data set that spans the period July 1981 to September 1994. The time series of normalized difference vegetation index (NDVI) data for land areas north of $45°$ N assembled by correcting the PAL data with spectral methods confirms the northerly greening trend and extension of the photosynthetically active growing season. Analysis of the channel reflectance data indicates that the interannual changes in red and near-infrared reflectances are similar to seasonal changes in the spring time period when green leaf area increases and photosynthetic activity ramps up. Model calculations and theoretical analysis of the sensitivity of NDVI to background reflectance variations confirm the hypothesis that warming driven reductions in snow cover extent and earlier onset of greening are responsible for the observed changes in spectral reflectances over vegetated land areas.

Index Terms—AVHRR, interannual variability, normalized difference vegetation index (NDVI), vegetation dynamics.

I. INTRODUCTION

SEVERAL studies on the interannual variability of global vegetation activity have been made possible with the availability of multiyear normalized difference vegetation index (NDVI) data in the mid-1990s [1]–[8]. The Pathfinder AVHRR Land (PAL) [9] and the Global Inventory Monitoring and Modeling Systems (GIMMS) [10] data are two of the more commonly used data sets. These coarse resolution (6–8 km) global data sets have a temporal frequency of 10–15 days. The length of the record depends on the data set, but they typically begin from July of 1981. Analyses of these data revealed large-scale interannual variations in global vegetation activity related to climate. For example, NDVI anomalies in semi-arid tropics have been reported to correlate well with equatorial Pacific sea surface temperature anomalies associated with the El Nino Southern Oscillation phenomenon [11]. In the northern latitudes, the NDVI data indicate a warming driven greening trend [12] consistent with observations of increased amplitude of the seasonal cycle of atmospheric CO_2 data from the north [13].

The processing of AVHRR data from different satellites to produce a calibrated time series of NDVI is a challenging task. The data lack critical corrections for aerosol scattering and water vapor absorption. Orbital drift and lack of on-board calibration further impact the quality of the time series. Nevertheless, several different correction methods have developed, tested and applied to the raw data to produce a consistent and calibrated time series. These include vicarious calibration techniques [14], [15], corrections for sun angle changes associated with orbital drift [16], compositing techniques that minimize atmospheric and bidirectional effects [17], and explicit corrections for stratospheric aerosol obscuration [18].

The northern latitude greening trend inferred from PAL and GIMMS NDVI data [12] has since been confirmed by several other investigations [19]–[22]. One study, however, questioned the reliability of NDVI data for inferring these changes [23]. The effects of orbital drift and sensor changes on channel 1 and 2 reflectances and NDVI from the PAL data set were recently investigated by Kaufmann *et al.* [24]. Based on theoretical and statistical analyses, they concluded that PAL NDVI data were not corrupted significantly by these effects and as such, the NDVI data could be used to infer interannual variability in global vegetation activity. In this article, we report on our investigations with the PAL data set for the period July 1981 to September 1994 along three lines. First, on the development of an improved NDVI data set from the PAL data and the inferred changes in vegetation growth in the north. Second, on the analysis of PAL channel 1 (red) and 2 (near-infrared) data in order to understand the mechanisms responsible for the NDVI change in the north. Third, on the interpretation of observed channel reflectance changes in terms of radiation transfer in vegetation media.

II. DATA AND METHODS

Global data sets of land surface temperature, biome classification, AVHRR channel reflectances and normalized difference vegetation index (NDVI) for the period July 1981 through June 1994 were used in this study. The NASA GISS land surface temperature data are gridded values at $2°$ spatial resolution [25]. The data are monthly anomalies with respect to 1951–1980 monthly mean temperatures.

The biome map used in this study is a classification of global vegetation into six distinct canopy structural types [26]. These are grasses and cereal crops, shrubs, broadleaf crops, savannas, broadleaf forests and needle forests. In this study, we focus on cool grasses and needle forests of the northern latitudes, that is Biomes 1 and 6. The grasses are distinguished
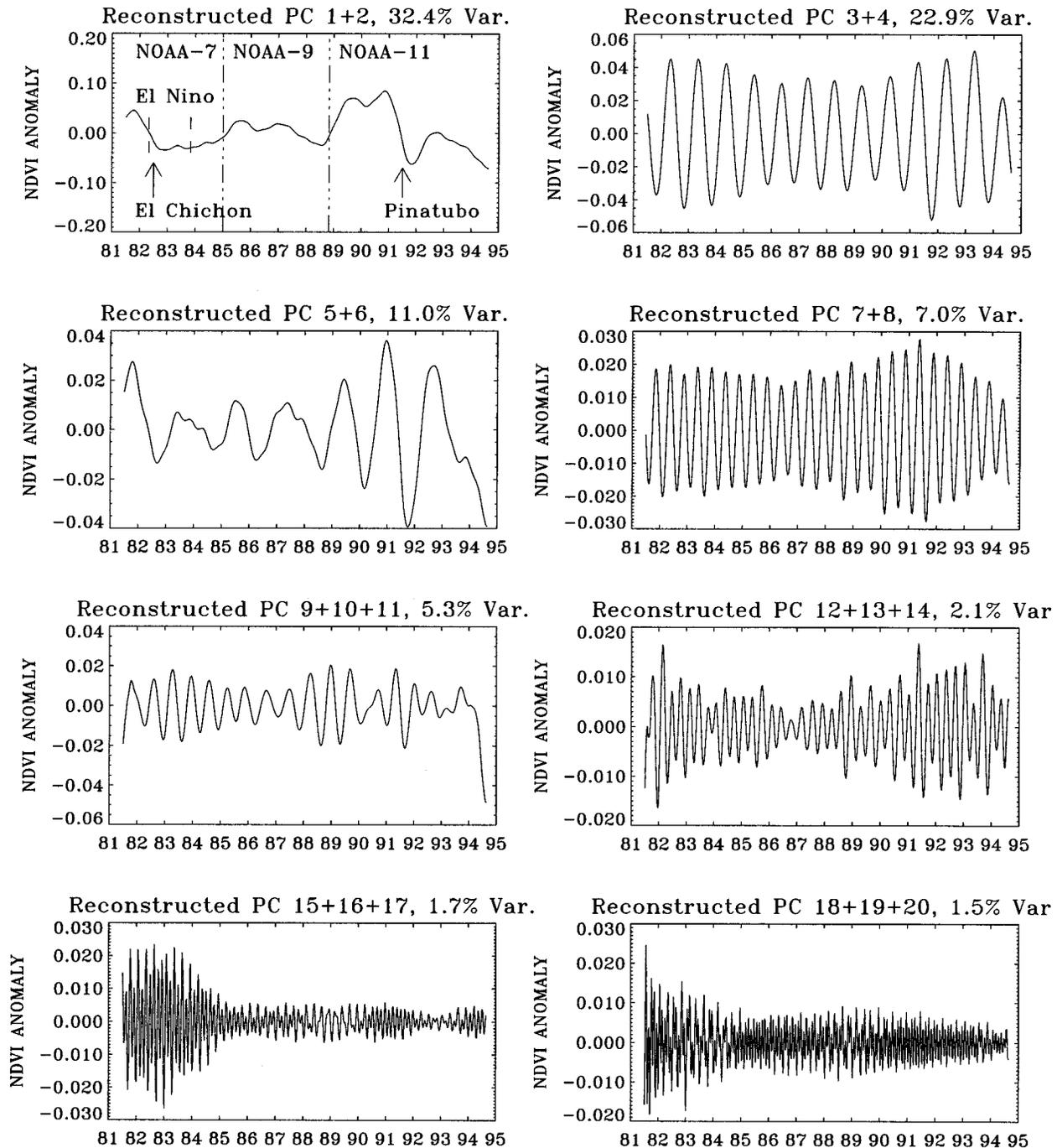
Fig. 1. Singular spectrum analysis of the time series of 5° latitudinal band NDVI anomaly. The panel shows a selection of the first 20 reconstructed principal components from SSA of the time series of spatially averaged PAL NDVI anomaly of vegetated pixels in the tropical band 5° S to 0°. Here, reconstructed principal components with similar spectral characteristics were grouped together. Window length was set to 90 (90*10 days ≈2.5 years) to primarily resolve periods at seasonal to interannual time scales.

by canopy vertical and lateral homogeneity, complete ground cover, short canopy, erect leaf orientation, minimal foliage clumping and growing on soils of intermediate soil brightness. The needle forests, on the other hand, are distinguished by needle clumping on shoots, shoot clumping in whorls, dark vertical trunks, green understorey during the growing season, else dark litter, and crown mutual shadowing. A decision tree classification algorithm was used to generate the biome map from AVHRR NDVI data of year 1995 at 1 km resolution [27]. The site-based accuracy of this map is 73%.

The data set of AVHRR channel reflectances was produced from the afternoon viewing NOAA series satellites (NOAA 7, 9, and 11) under the joint sponsorship of NASA and NOAA Earth Observing System Pathfinder project [9]. The spectral channels have the following characteristics: channel 1 is the 580–680 nm wavelength band (red band) and channel 2 is the 725–1100 nm wavelength band (near-infrared band). The data processing included improved navigation, inter-satellite calibration and partial correction for Raleigh scattering. The nominal resolution of the data is 8 km and the temporal frequency is ten days.
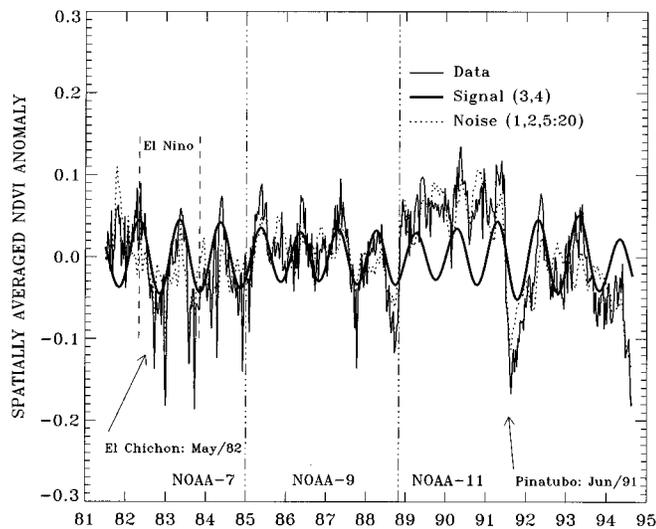
Fig. 2.   PAL ten-day NDVI anomaly time series (data) for vegetated pixels in the tropical band 5° S to 0° and aggregated PC components denoting noise and signal. Numbers in brackets indicate the number of the PCs from Fig. 1. The large amplitude noise in these tropical vegetation data is due to residual cloud effects in the PAL NDVI data. Note also the impacts of stratospheric aerosols effects due to Mount Pinatubo eruption in June of 1991 and the dramatic loss of orbit in 1994.

The channel data were used to evaluate NDVI, defined as (nir − red)/(nir + red), where nir and red are near-infrared (channel 2) and red (channel 1) reflectances. The NDVI is expressed on a scale from −1 to 1. For green vegetated surfaces, near-infrared reflectance is always greater than red reflectance and therefore NDVI > 0. The utility of NDVI data for studying global vegetation dynamics has been well documented [11], [28], [29]. NDVI data are generally found to be well correlated to the fraction of photosynthetically active radiation (400–700 nm) absorbed by green vegetation [30]. Its time integral is a good predictor of carbon fixation and primary productivity [31]. In fact, it can be rigorously shown using radiative transfer theory that NDVI is indicative of abundance and activity of leaf chlorophyll pigments [32].

Complete coverage of the land surface is possible daily with AVHRR sensors. The daily data can be of poor quality because of atmospheric conditions (clouds and aerosols). Atmospheric degradation of the surface signal is such that it tends to enhance the surface reflectance at red and decrease it at near-infrared channel [33]. Over the course of few days, during which if the surface is assumed to be invariant, the maximum value of NDVI during this period generally corresponds to the clearest atmosphere and to near nadir viewing angles, slightly about the forward scattering directions [17]. In the case of the Pathfinder data set, this compositing period corresponds to ten days and three composites for each month. Maximum value NDVI compositing minimizes, but not eliminates, residual atmospheric and bidirectional effects. Residual noise due to orbital drift, inter-sensor variations and stratospheric aerosol effects during the period following the eruption of Mount Pinatubo (June 1991) in the data have been reported [12]. The NDVI data were corrected as follows.

The time series of NDVI for barren and vegetated pixels in 5° latitude bands were extracted from a 0.25° NDVI data set,

created by aggregating the 8 km data, using the land cover classification map described earlier. The spatial aggregation over the specific surface types emphasizes temporal variations in the NDVI fields, which is the focus here. After subtracting the mean, based on the full record length, each of the resulting spatially averaged NDVI anomaly time series was subjected to singular spectrum analysis (SSA), which is a form of principal component analysis in the time domain [34], [35]. The first 8 principal components (PCs) generally accounted for about 95% of the variance in the series. These components were then grouped into either noise or signal based on information from sun angles, volcanic eruptions (El Chicon and Mount Pinatubo), sensor changes and physics of radiative transfer. However, significant high frequency noise in the PAL NDVI tropical data, mainly as a result of residual cloud contamination, required inclusion of a larger number of PCs. For example, Fig. 1 shows the first 20 reconstructed principal components for all vegetated pixels in the tropical band 5° S to 0°. The sum of the reconstructed PCs 3 and 4 shows the expected regularly recurring annual cycle corresponding to wet and dry periods. In contrast, the reconstructed PCs 1 and 2 as well as 5 and 6 capture well degradation due to stratospheric aerosols (Pinatubo, El Chicon), intersensor variations, and effects of orbital loss at the end of the satellites lifetime [12]. Effects of the movement of the ITCZ and associated change in atmospheric water vapor content on the NDVI data in this tropical band are likely to be captured in the sum of the reconstructed PCs 7 and 8 [16]. The remaining PCs explain only a small portion of the variances in the PAL NDVI data and mostly capture high frequency variations from residual cloud contamination. The PAL NDVI anomaly time series for this tropical band and the aggregated reconstructed PCs denoting noise and signal are shown in Fig. 2. The latitude and surface specific noise time series were then used to correct the 0.25° and 8 km time series of all pixels in each 5° latitude band. As an example, raw data, signal and noise for the 45°–50° N band are shown in Fig. 3 at 8 km and 0.25° resolutions. The corrections are clearly better in the 0.25° NDVI data set as the noise series corresponds to the aggregate noise in that band. Nevertheless, the improvement in data quality can be seen, with important residual errors in the processed data set corrected. The improved NDVI data is referred to as the improved Pathfinder NDVI data set in this article.

III. UPDATE ON NDVI CHANGES IN THE NORTHERN LATITUDES

In recent articles [4], [12], Myneni *et al.*have reported that the photosynthetic activity of terrestrial vegetation increased from 1981 to 1991 in a manner suggesting an increase in plant growth associated with an increase in the duration of the active growing season based on analysis of two vegetation index data sets (the Pathfinder AVHRR land data set and the GIMMS data set). The regions of greatest increase were found to be within the 45°–70° N latitudinal where marked warming occurred in the spring time due to an early disappearance of snow [36], [37]. The seasonal amplitude of NDVI was reported to have increased by about 10% accompanied by an increase in the length of the active growing season by about 12 ± 4 days. The satellite data were
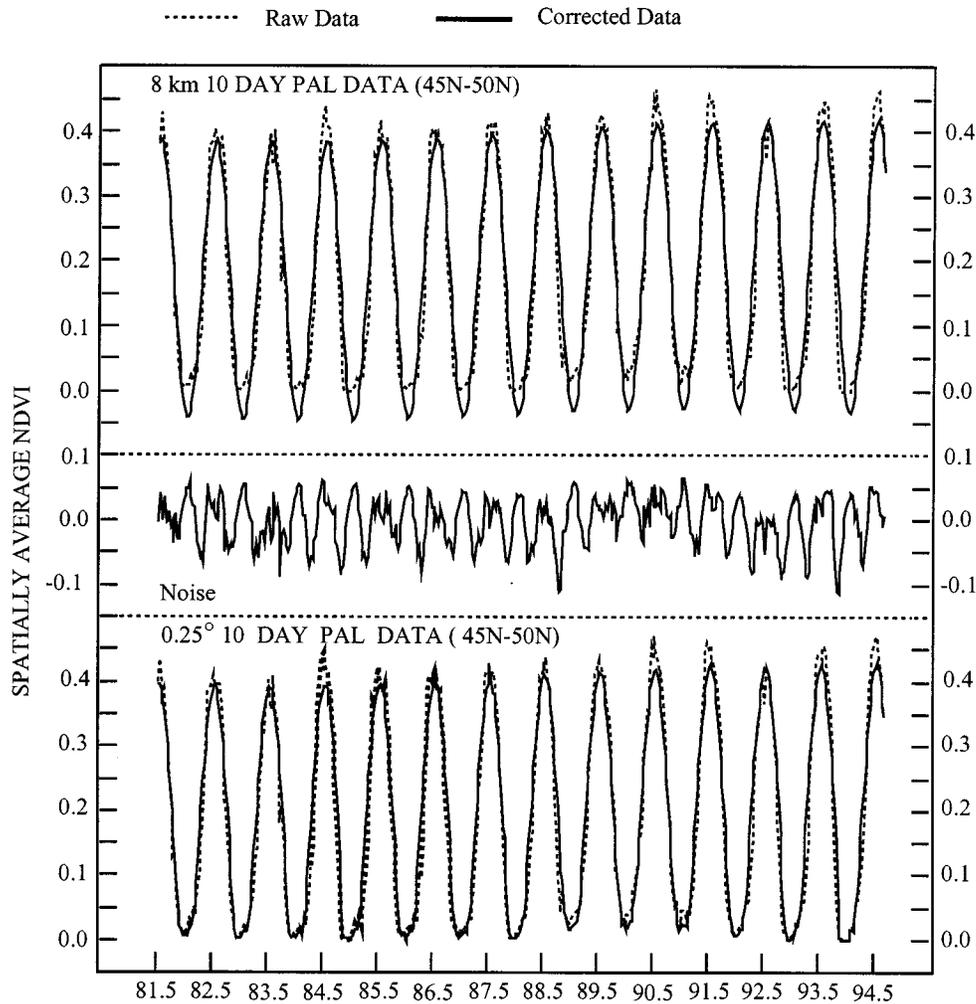
Fig. 3.   Corrected and uncorrected NDVI time series for the 45° N–50° N latitudinal band. Corrections to the 8 km and 0.25° data are shown in the top and bottom panels, respectively. Although the noise series (middle panel) was developed from the 0.25° data, the corrections reasonably well translate to the 8 km pixel resolution.

concordant with an increase in amplitude of the seasonal cycle of atmospheric CO_2 exceeding 20% since the early 1970s, and an advance in the timing of the drawdown of CO_2 in spring and early summer of up to seven days [13]. They conclude that both the vegetation index data and the CO_2 record indicate that the global carbon cycle has responded to interannual fluctuations in temperature, which, although small at the global scale, were regionally highly significant.

Several more recent studies have confirmed the northern latitude greening trend and the extension of the growing season [19]–[22]. One study, however, questioned the reliability of NDVI data for inferring these changes, especially due to potential artifacts in the data related to satellite orbital drift and intersensor changes [23]. Moreover, Myneni *et al.*have not analyzed the component channel data, which could have provided insight into the noise versus signal issues. Here, we first repeat the analysis of Myneni *et al.* [4] with the improved NDVI data described earlier, for the entire period of the record, July 1981 through September 1994, in order to confirm the published findings, and second, we analyze the channel data to explain the greening trend in terms of mechanisms which have a basis in radiation transfer theory.

The effect of changes in solar zenith angle (orbital drift) and sensor changes (intersensor variations) on channel 1 and 2 reflectances and NDVI from the AVHRR Pathfinder Land data set for the period July 1981 to September 1994 is addressed in Kaufmann *et al.* [24]. Briefly, it was shown that the NDVI of a vegetated surface is a function of the maximum positive eigenvalue of the radiative transfer equation. A sensitivity analysis of this relation indicates that NDVI is minimally sensitive to sun angle changes and this sensitivity decreases as leaf area increases. Statistical methods were also used to analyze the relationship between sun angle, AVHRR channel reflectances and NDVI. It was shown that the use of ordinary least squares could generate spurious regressions because of the nonstationary property of time series. To avoid such confusion, the notion of cointegration was used to analyze the relation between solar angle and AVHRR data. The results were consistent with the conclusion of theoretical analysis from equations of radiative transfer. NDVI is not related to solar angle in a statistically significant manner except for biomes with relatively low leaf area. From the reported analysis [24], it is concluded that the Pathfinder AVHRR Land NDVI data were not contaminated by trends introduced from changes in
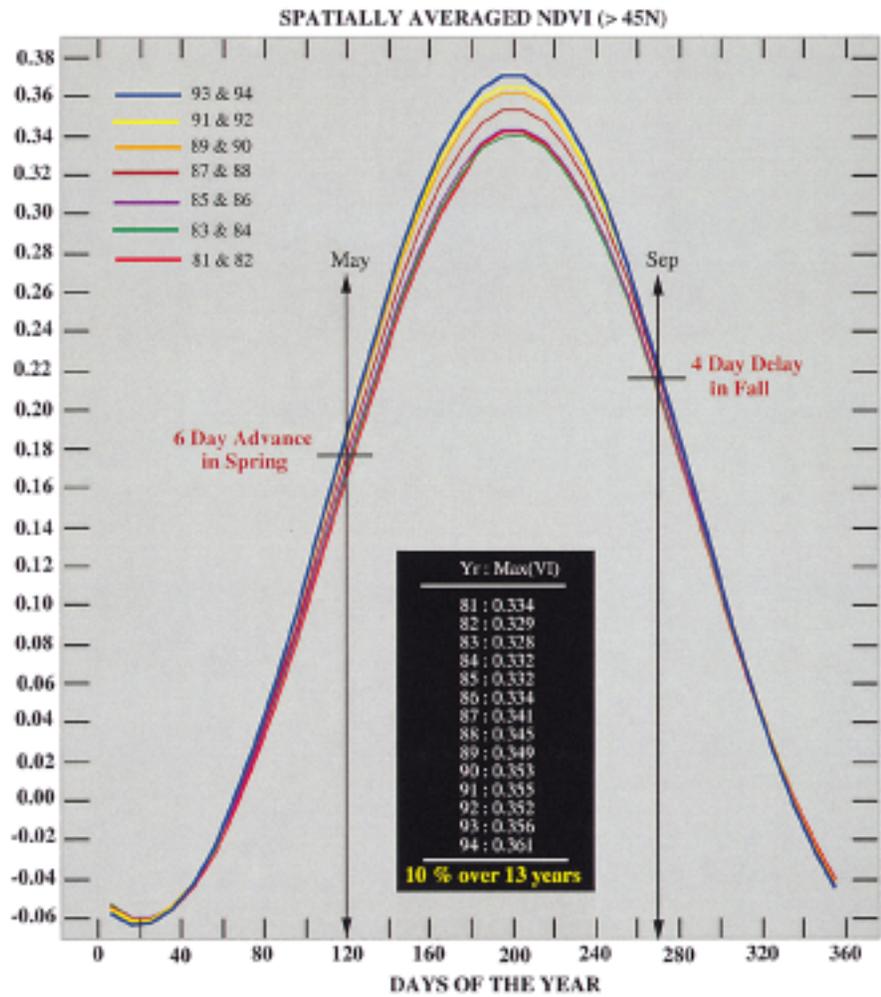
Fig. 4.   Annual course of NDVI from vegetated areas north of 45° N. Vegetated areas were delineated from barren areas by requiring that the 13-year monthly average NDVI be greater than 0.1 and be within plus or minus 3σ of the monthly average.

Fig. 5.   Map of the regions (red pixels) selected for investigation on the channel reflectance changes. In these regions, spring period (March to May) NDVI >0.1 and increased by at least 25% between 1982 and 1991, and the correlation between spring time NDVI and temperature was at least 0.5.

solar zenith angle due to orbital decay and changes in satellites (NOAA-7, 9, 11). As such, the NDVI data could be used to analyze interannual variability of global vegetation activity.

We repeated the analysis reported by Myneni *et al.* [4] with the improved NDVI data set. The annual course of NDVI from vegetated areas north of 45° N is shown in Fig. 4. Vegetated areas were delineated from barren areas by requiring that the 13-year monthly average NDVI be greater than 0.1 and be within plus or minus 3σ of the monthly average. The first condition guaranteed that bare and sparsely vegetated pixels were

excluded, and the second condition ensured that snow covered areas and bad scan-lines were excluded. The curves shown in Fig. 4 are biyearly averages of successive years, starting from the beginning of the record; shown thus for clarity. The timing of the onset of the growing season was inferred by the change in NDVI of these bi-yearly curves on day 120. That is, a threshold NDVI value was defined as the NDVI value on day 120 of the mid-point of the record (1987–1988 curve) and the advance in spring time onset of greenness evaluated as the difference in time between the bi-yearly curves from 1993–1994 and 1981–1982 (see Fig. 4). The delay in the decline of autumn greenness was likewise inferred on day 270, about the end of September. From this analysis, we infer a six-day advance in the onset of greenness and a four-day delay in the decline of autumn greenness during the 1981–1994 period. An increase of about 10% in the amplitude of the seasonal NDVI course was also inferred from the changes in peak NDVI values shown in Fig. 4. Both the timing and amplitude results are broadly consistent with the published finding of Myneni *et al.* [4]. It should be emphasized that the magnitude of these changes should be interpreted with caution because of the lack of explicit atmospheric corrections and on-board calibration. Further, NDVI data are only surrogates of plant photosynthetic activity and the translation to actual photosynthetic gains requires additional research. We now inquire into the basis for the observed changes in NDVI by analyzing the component channel data.

IV. AVHRR CHANNEL 1 AND 2 DATA ANALYSIS

A. Selection of Study Area

The northerly latitudes (23.6° N–90° N) have warmed by about 0.8 °C since the early 1970s but not all areas have warmed uniformly [25]. The warming is pronounced during the cool seasons, especially in the spring period, due to the positive feedback associated with the decline in the extent of snow cover [37]. This warming is believed to have caused progressively earlier onset of spring greening in the seasonal vegetation of the north [4]. In order to better understand the mechanism of these changes, we studied the component channel reflectance data in addition to NDVI. This we did by first selecting focused regions for investigation. We selected areas where during the spring period (March to May) NDVI > 0.1 and increased by at least 25% between 1982 and 1991, and the correlation between spring time NDVI and temperature was at least 0.5. The resulting mask (red areas) is sown in Fig. 5. Most of the pixels thus selected form one large patch (45 358 pixels in total) in Northern Europe and Scandinavia between 50°–70° N. A few clusters of pixels are seen in North America but these are spatially incoherent. This explains our choice to restrict analysis to data from Europe and Scandinavia only. Channel data provide more information than an index such as NDVI. Inclusion of channel data justifies performing separate analysis for structurally different biomes. This is in contrast to our previous NDVI data analysis, which was performed for all biomes together. Separate study can help distinguish signatures of interannual variations in spectral space for different vegetation types. The global biome mask was used to identify structurally distinct vegetation types in the selected

TABLE I
BIOME TYPE DISTRIBUTION IN THE REGIONS SELECTED FOR CHANNEL INVESTIGATION SHOWN IN FIG. 4. THE COLUMNS FRACTION >1/64 AND FRACTION >50/64 INDICATE THE HOMOGENEITY OF 1 km BIOME PIXELS IN THE 8 km REFLECTANCE PIXELS

	Fraction> 1/64	Fraction>50/64
Grasses	34,799	7,888
Shrubs	3,044	141
Broadleaf Crops	6,512	166
Savannas	37,233	3,108
Broadleaf forests	16,179	1,226
Needle forests	26,615	4,456
Total number of pixels	45,358	

regions. As the biome map was at a finer resolution (1 km) compared to the PAL data (8 km), we selected pixels for investigation based on biome homogeneity, for example, by requiring that 50 of the 64 1 km pixels belong to the same vegetation type. The consideration of homogeneity was needed because only those pixels with high homogeneity will exhibit properties of a particular vegetation type. Also, the effect of misclassification on our analysis will be reduced. As shown in Table I, the two most predominant biome types in the study area are cool grasses and needle leaf forests. All further analysis was restricted to Pathfinder AVHRR Land channel data from homogeneous pixels of these two biomes for the period July 1981 to June 1991 (to exclude corrupted data due to eruption of Mount Pinatubo).

B. Interannual Variations

We focus our analysis on data from three spring months—March, April and May. The analysis was performed with monthly data without averaging over whole season, because of rapid changes in greenness (and channel reflectances) during these months. Additionally, the monthly data during the 1980s represent realizations of springtime vegetation activity generated by an inherently chaotic climate system [38]. Therefore, instead of comparing, say March 1982 with March 1991, we regress the ten realizations (corresponding to the ten years) for the month of March, and use the regression-predicted end values of this period in our analysis. We implemented several techniques to analyze possible trends in data and discuss these below.

Contour plots of the density of regressed channel data in the red and near-infrared space are shown in Fig. 6 for April 1982 and 1991, for the two biomes. The contours enclose approximately 50% of all data with highest density. Although the data contours of the two biomes overlap considerably, the tendency for change from 1982 to 1991 is different. In the case of grasses, red reflectances decrease slightly while near-infrared reflectances increase. In needle forests, both channel reflectances decrease. It is important to note that the total number of data in both years was constant in each biome, so the plots shown in Fig. 6 are directly comparable.

Histograms depicting the distribution of red and near-infrared reflectances of grasses for the months of March and April are shown in Fig. 7, separately for the years 1982 and 1991. Similar plots for needle forests are shown in Fig. 8. Again, we see that in the case of grasses, red reflectances decrease slightly
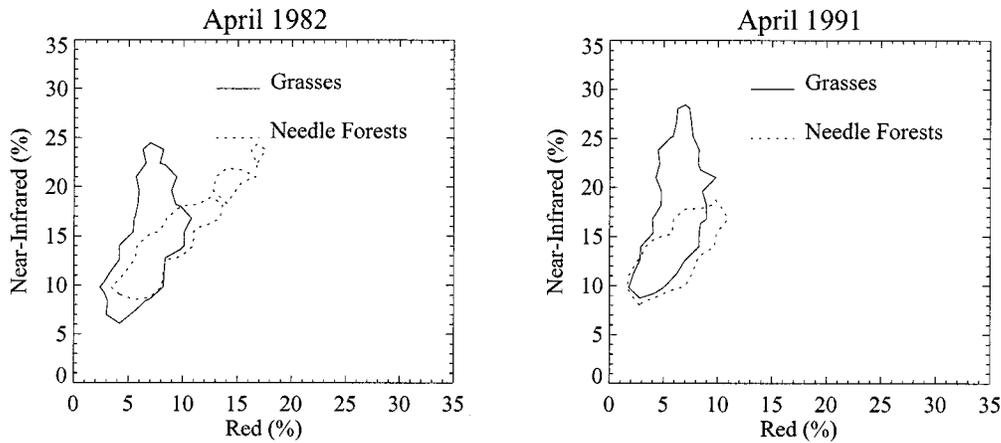
Fig. 6. 50% density contours of the regressed channel data in red and near-infrared space for grasses and needle forests for April 1982 and 1991.
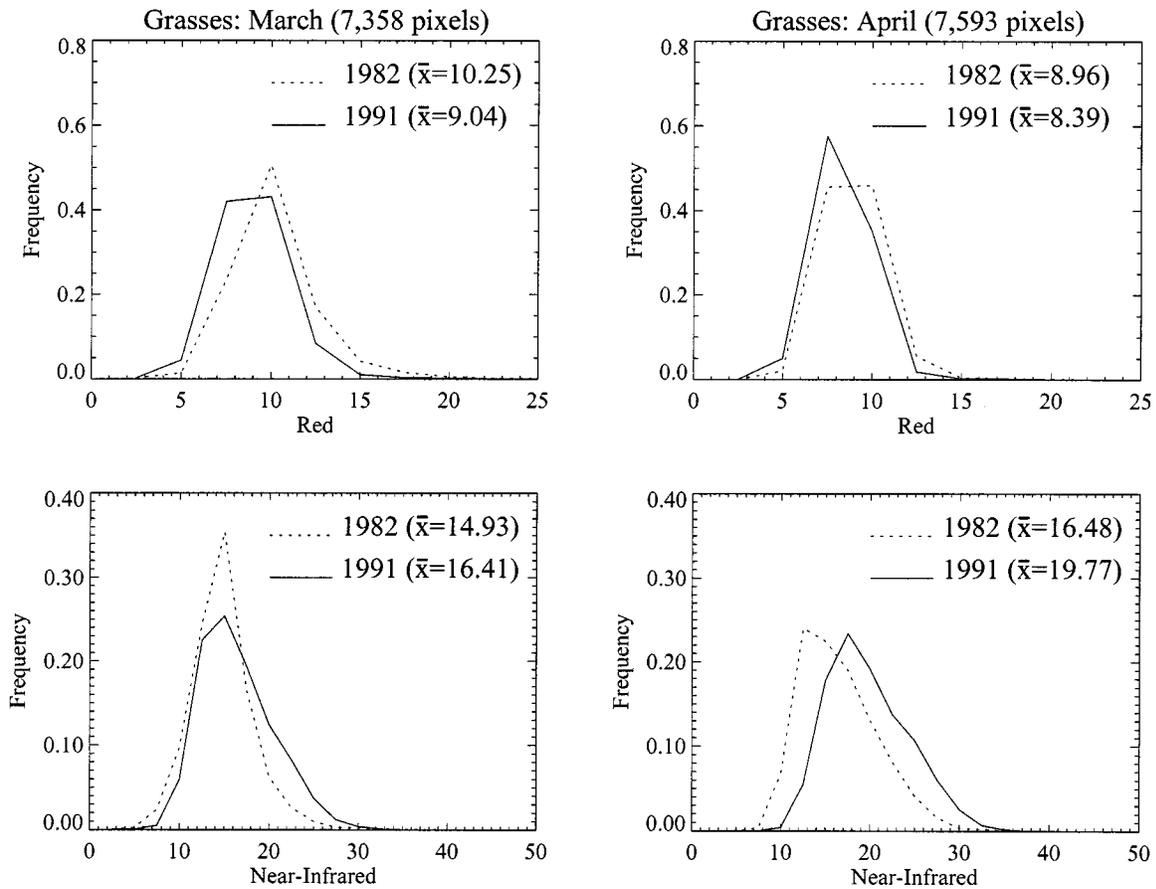
Fig. 7. Distribution of regressed red and near-infrared reflectances (%) of grasses for March and April for 1982 and 1991. Mean of the distribution is denoted by $\bar{x}$.

(from 10.25 to 9.04 in March and from 8.96 to 8.39 in April; all reflectances are in %) and near-infrared reflectances increase (from 14.93 to 16.41 in March and from 16.48 to 19.77 in April) during the 1982 to 1991 period. In needle forests, the profile of distribution changes significantly both at red and near-infrared channels, especially in March. Thus, red reflectance decreases from 20.39 to 14.28 in March and from 12.08 to 8.82 in April and near-infrared reflectance decreases from 26.70 to 21.30 in March and from 17.67 to 16.13 in April.

It is of interest to investigate the direction and magnitude of change in the data in the two-dimensional (2-D) red/near-infrared space, separately for the two biomes. To represent the observed interannual variations, we evaluate vectors of change $(\Delta red_{interannual}, \Delta nir_{interannual})$, defined as

$$\Delta red_{interannual} = red_{91} - red_{82},$$

$$\Delta nir_{interannual} = nir_{91} - nir_{82} \qquad (1)$$
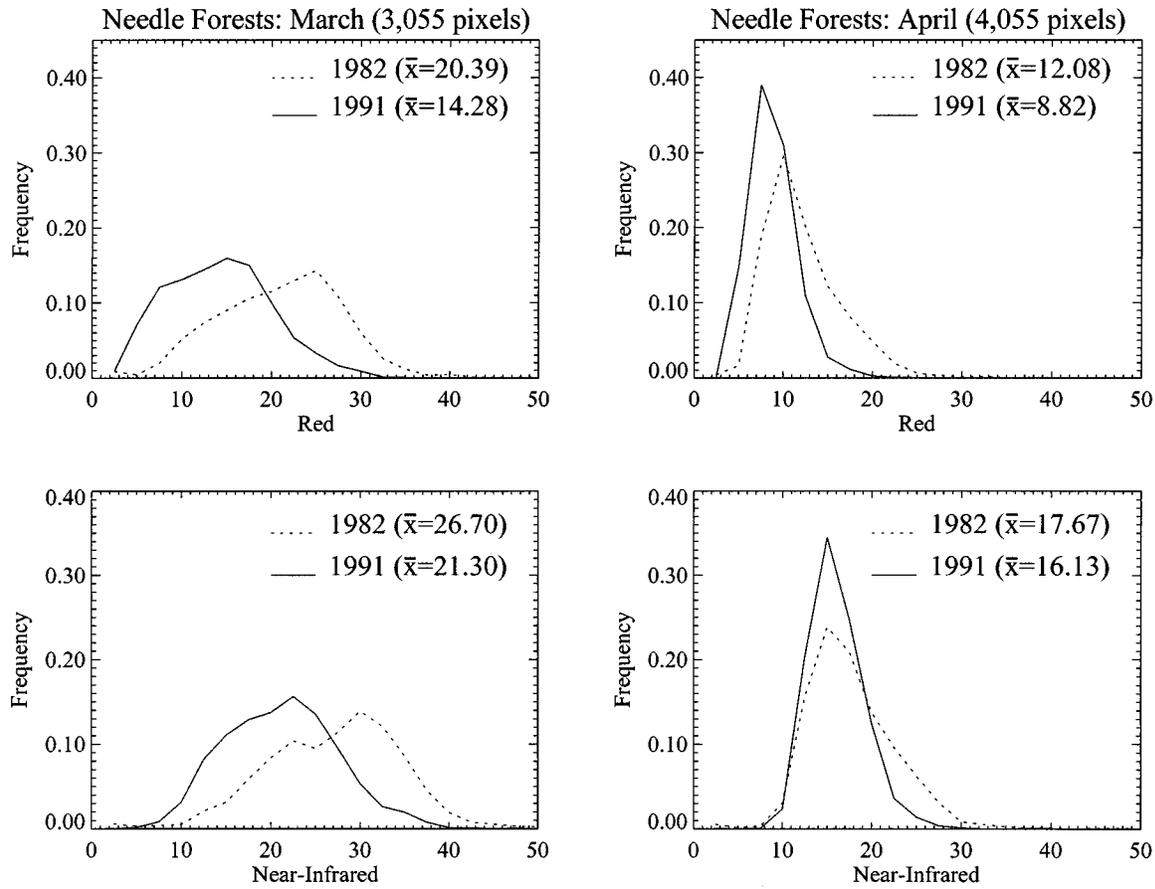
Fig. 8.   Distribution of regressed red and near-infrared reflectances (%) of needle forests for March and April for 1982 and 1991. Mean of the distribution is denoted by $\bar{x}$.

where red_{91}, for example, represents regressed channel 1 reflectance in 1991 during a specific month (March, April or May). The vectors are represented by their norm, here termed distance, and angle with respect to the red reflectance axis. The vectors were calculated for all pixels in the study region, separately for the three spring months. From this vector set, the distributions of distances and angles were evaluated. Results for the months of March and April are shown in Figs. 9 and 10 for the two biome types. These distance and angle distributions correspond to changes in the channel data between the years 1982 to 1991 during a particular month (March and April). The distribution of distances shown in the lower panels have a distinct peak indicating that in both biome types, the most probable movement is about 3–7% reflectance units (which compares well with the mean value changes discussed earlier), during both months. Had the interannual variations in channel data been due to artifacts, i.e., not causal, one would expect this distribution to be more uniform.

Polar plots shown in the upper panels of Figs. 9 and 10 depict both the angle with respect to the red axis and the probability density for this direction to occur by the radius. Two different signatures of change in the spring time can be noted from these figures; one is location at the boundary between the first and second quadrant while the other in the third quadrant. Needle forests exhibit evolution of only one signature—a well-defined spike in the third quadrant in March, somewhat spread over the adjacent directions in April. In the case of grasses the probability

of location in the third quadrant decreases and the probability of location near the boundary between the first and second quadrant increases during the transition from March to April. Analysis of data for all months of the year indicates that these signatures have a strong seasonal dependency. The probability of location in the third quadrant increases through the cool season (October to March) and then decreases in the transition to the warm season, while the other signature has the opposite evolution. The difference between the two biomes is just variation of this general order. We will attempt to explain both signatures with the aid of radiative transfer theory in the next subsection. Finally, note that in Figs. 9 and 10 for both biome types, quadrant IV in polar plot is always empty, because the data selected for this analysis is from areas where NDVI has increased (cf. next section).

The results shown earlier characterize the aggregate movement over time in the 2-D spectral space. It is also of interest to see the details of change as function of location in the spectral space, i.e., vector field of changes. This is shown in Fig. 11 for the period April 1982 to April 1991. The spectral space shown contains a high density of channel data, as can be ascertained from Fig. 6, and generally corresponds to red reflectances $\in[5:15\%]$ and near-infrared reflectances $\in[5:30\%]$. The movement in the spectral space in the case of grasses is a result of increasing near-infrared reflectance when red reflectance is low (less than 10%). On the other hand, when red reflectance is high, the movement is a result of decrease in both red and
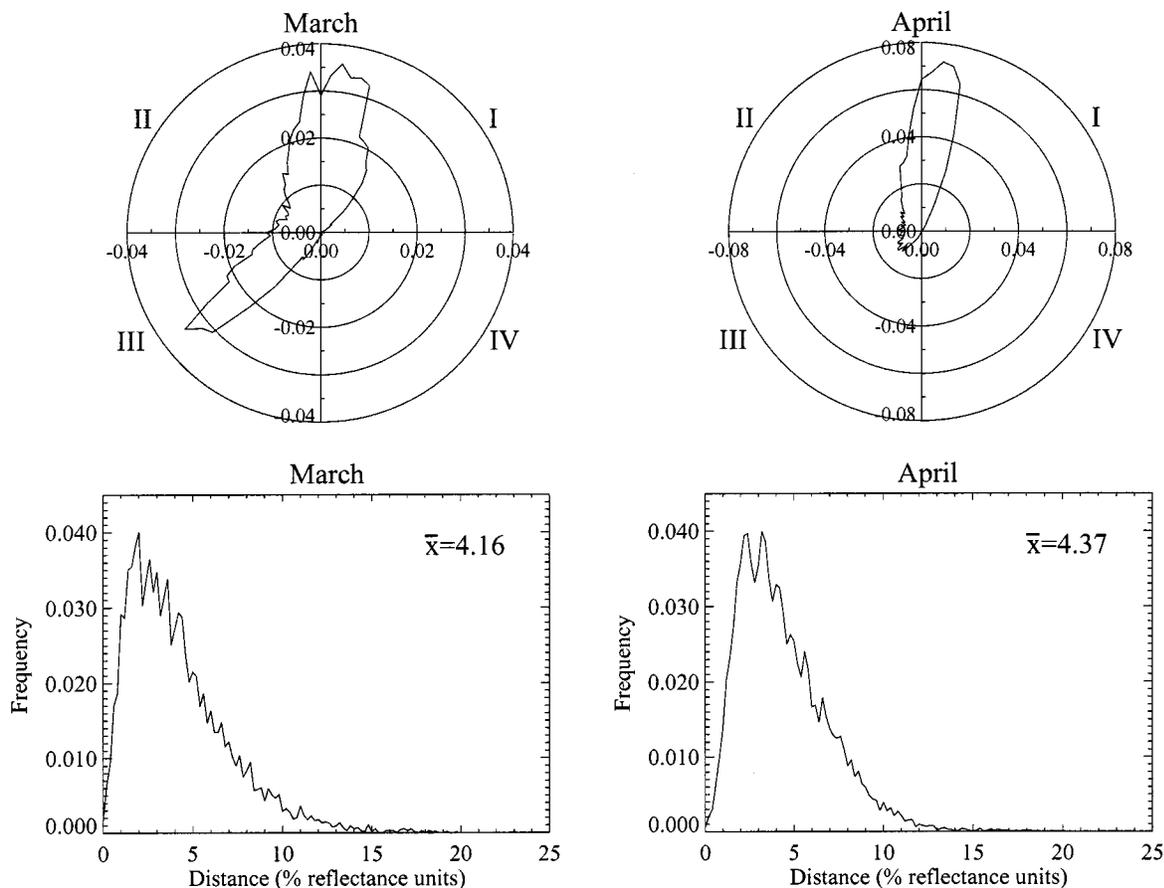
Fig. 9. Distribution of the change vector magnitude, here termed distance, and direction, in grasses from 1982 to 1991. The polar plots in the upper panels depict both the angle with respect to the red axis and the probability density for this direction of change to occur by the radius.

near-infrared reflectances. The former accounts for the upward direction of movement of reflectances in Fig. 9 and, the latter for movement in the third quadrant. In the case of needle forests, the movement is uniform throughout the spectral space.

In conclusion, several techniques of channel data analysis at the interannual scale show that during the spring period, NDVI increase in the case of grasses is predominantly due to an increase in near-infrared reflectances, but in needle forests the NDVI increase is a result of decrease in both red and near-infrared reflectances. In the next section, we investigate channel reflectance changes at a shorter temporal scale; seasonal, in order to contrast those with changes at the interannual scale.

C. Seasonal Variations

The increase in green leaf area and ramping of photosynthetic activity in the spring time period is captured prominently by the NDVI data, as has been noted in many previous studies, for example [10]. But it is instructive to investigate the associated changes in component channel reflectances and compare these with interannual variations. Spring is represented here as the period from March to May. The years 1982 and 1989 were chosen to document these seasonal changes. Changes in red and near-infrared reflectances were evaluated as

$$\Delta \text{red}_{\text{seasonal}} = \text{red}_{\text{may}} - \text{red}_{\text{mar}},$$

$$\Delta \text{nir}_{\text{seasonal}} = \text{nir}_{\text{may}} - \text{nir}_{\text{mar}}. \qquad (2)$$

The results are shown in Fig. 12 as vector fields of changes in the spectral space. In both years, the pattern of seasonal changes does not change much in each biome. In grasses, we note an increase in near-infrared reflectance and a slight decrease in red reflectance, while in needle forests, a decrease in both red and near-infrared reflectances. Also, in case of grasses the vector fields occupy a significantly larger space with higher values of near-infrared reflectances because of an interannual drift in this direction. Thus, potentially an important conclusion can be drawn—the seasonal pattern of change is qualitatively similar to the aforementioned interannual changes, although the magnitude of seasonal changes is large compared to the interannual changes. So, with passage of time, the measurements at the same time of the season indicate later and later phases of spring time greenness. This can be formulated equivalently as onset of spring time green-up progressively earlier during the ten years of analysis. Since seasonal changes are a result of decreasing snow cover and increasing green leaf area, we propose that the interannual changes are also caused by the same factors.

D. Theoretical Analysis

Analysis of the improved NDVI data set indicates an earlier onset of spring in the northern latitudes and a greening trend of about 10% during the 1981–1994 period (Fig. 4). An investigation of the channel data confirm this and reveals that interannual changes in spectral space are similar to the seasonal changes, but
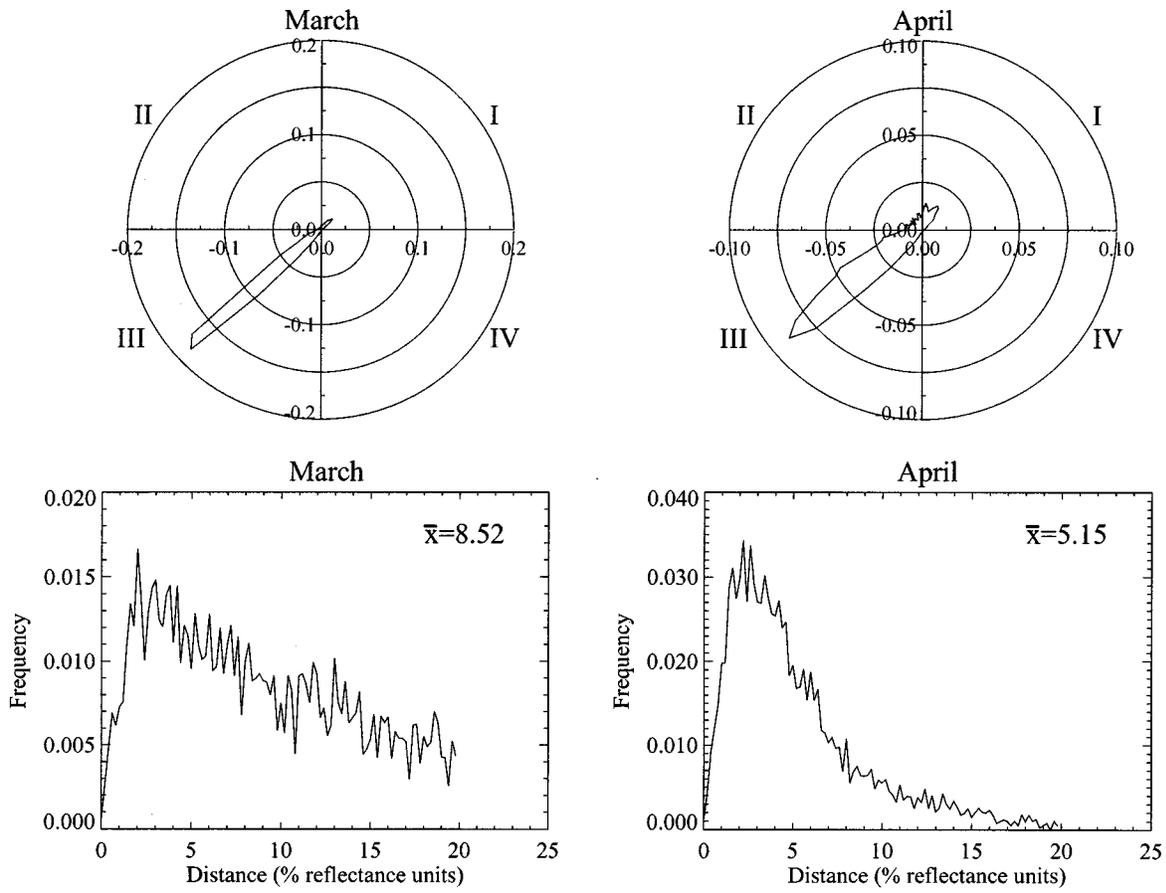
Fig. 10. Distribution of the change vector magnitude, here termed distance, and direction, in needle forests from 1982 to 1991. The polar plots in the upper panels depict both the angle with respect to the red axis and the probability density for this direction of change to occur by the radius.
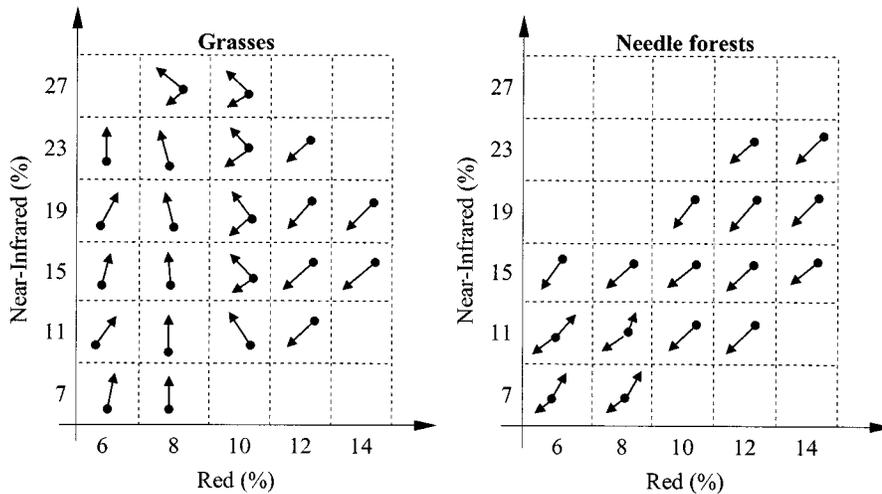
Fig. 11. Vector field of interannual changes in the spectral space. Vectors in each cell denote the direction of change from April 1982 to April 1991. Empty cells indicate insufficient data.

that the NDVI increase is due to different changes in the component channel reflectances depending on the biome type. We now attempt a theoretical explanation of these empirical results using radiative transfer theory.

We first identify domains in the spectral space where changes in red and near-infrared reflectances can result in either an increase or decrease of NDVI. This is accomplished geometrically as follows. The NDVI isoline, a straight line, which passes through the origin is uniquely identified by angle of slope, α as (Fig. 13)

$$\mathrm{NDVI} \equiv \frac{\mathrm{nir} - \mathrm{red}}{\mathrm{nir} + \mathrm{red}} = \frac{\mathrm{nir/red} - 1}{\mathrm{nir/red} + 1} = \frac{\mathrm{tg}(\alpha) - 1}{\mathrm{tg}(\alpha) + 1} = \mathrm{f}(\alpha). \quad (3)$$

Now, consider an arbitrary initial location of red and near-infrared reflectance $(\mathrm{red}_0, \mathrm{nir}_0)$ on this line. This line bifurcates the spectral space such that any movement $(\mathrm{red}_0 + \Delta\mathrm{red}, \mathrm{nir}_0 +$
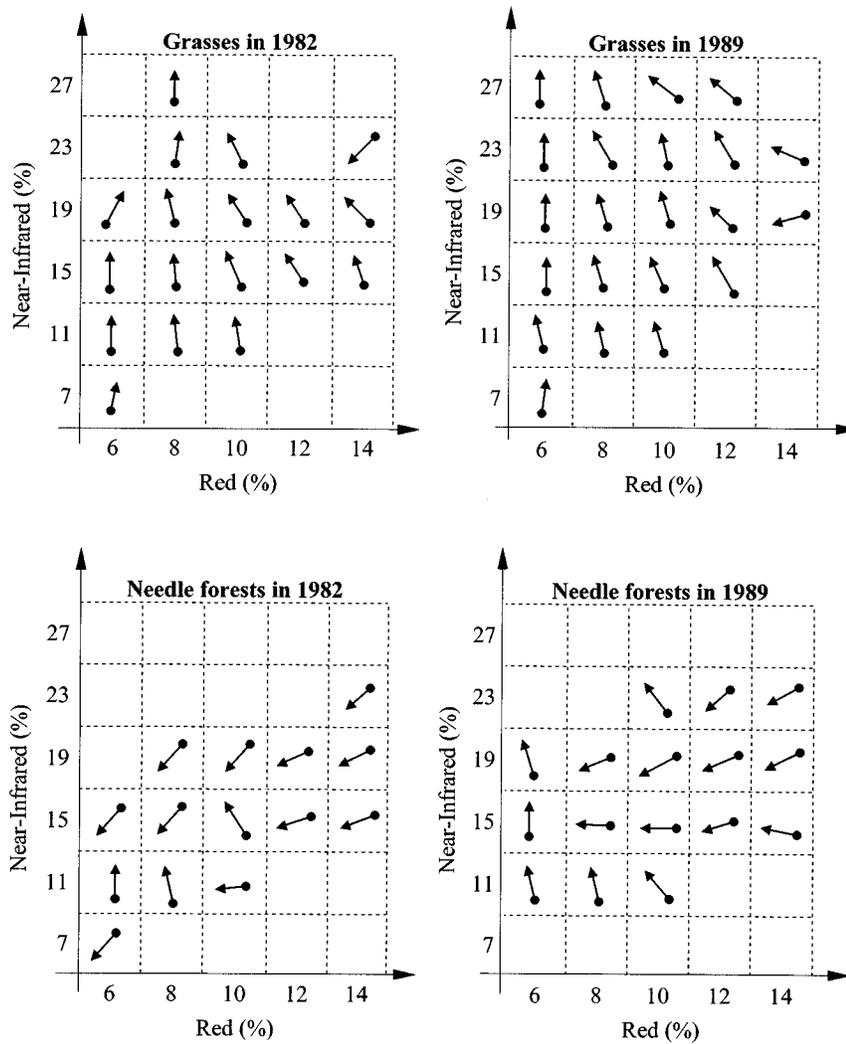
Fig. 12.   Vector field of seasonal change in the spectral space. Vectors in each cell denote the direction of change from March to May of the same year. Empty cells indicate insufficient data.
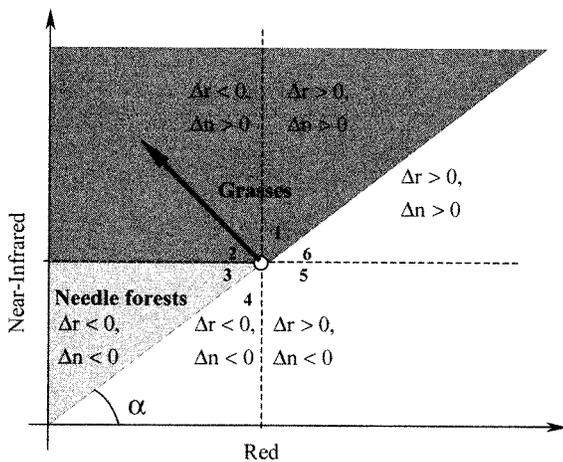
Fig. 13.   Schematic diagram of NDVI changes that result from changes in component channel reflectances (Δred; Δnir). Consider the initial location, as shown. The NDVI isoline connecting this point and the origin, at an angle α, bifurcates the spectral space such that sectors one to three correspond to NDVI increases should the end point of the change vector reside in here. Likewise, NDVI decreases in sectors four to six.

Δnir) into the sector earlier results in NDVI increase and vice versa, because NDVI is a monotonical function of the angle of slope, $\alpha(\partial \text{NDVI}/\partial \alpha > 0, \forall \alpha \in [0°; 90°])$. For clarity, we divide the spectral space into four more sectors, in each of which the sign of Δred and Δnir is constant. In total we have six different cases, which explains any possible variations in NDVI (cf. Fig. 13),

$\Delta\text{NDVI} > 0$, if

$$\begin{cases} 1)\Delta\text{red} > 0, \ \Delta\text{nir} > 0, \ \Delta\text{nir}/\Delta\text{red} > \text{tg}(\alpha(\text{NDVI})), \\ 2)\Delta\text{red} < 0, \ \Delta\text{nir} > 0, \\ 3)\Delta\text{red} < 0, \ \Delta\text{nir} < 0, \ \Delta\text{nir}/\Delta\text{red} < \text{tg}(\alpha(\text{NDVI})). \end{cases} \quad (4a)$$

and

$\Delta\text{NDVI} < 0$, if

$$\begin{cases} 4)\Delta\text{red} < 0, \ \Delta\text{nir} < 0, \ \Delta\text{nir}/\Delta\text{red} > \text{tg}(\alpha(\text{NDVI})), \\ 5)\Delta\text{red} > 0, \ \Delta\text{nir} < 0, \\ 6)\Delta\text{red} > 0, \ \Delta\text{nir} > 0, \ \Delta\text{nir}/\Delta\text{red} < \text{tg}(\alpha(\text{NDVI})). \end{cases} \quad (4b)$$

The channel reflectance changes shown in Figs. 9 and 10 can now be classified as follows. The change vector in the case of grasses corresponds to sectors one and two of Fig. 13, and in
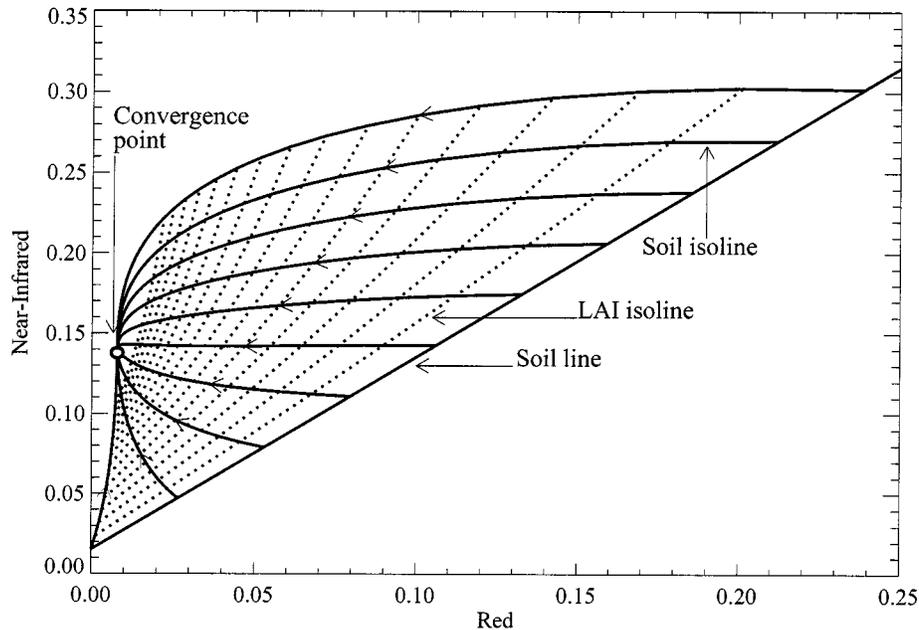
Fig. 14.   Solution of the radiative transfer model (BRF at nadir) for a wide range of LAI and background reflectances and fixed optical properties of canopy. When soil reflectance is constant and LAI is varying, the set of solutions define the soil isoline or trajectory (solid curves with arrow), which originates on the so-called soil line, where leaf area is zero (solid straight line) and converge to a common point, as leaf area tends to infinity. Note that for very dark backgrounds, increasing leaf area increases both red and near-infrared reflectances, while for backgrounds of intermediate brightness, red reflectance decreases and near-infrared reflectance increases. In the case of very bright backgrounds, increasing leaf area decreases both red and near-infrared reflectances. When LAI is constant and background reflectance is varying, the set of solutions define the LAI isolines (dashed curves).

needle forests to sector three. Clearly, in all these sectors, NDVI increases. In sectors four to six NDVI decreases, and since only those pixels which exhibit NDVI increase are considered, these sectors will always be empty, as can be seen in Figs. 9 and Fig. 10. Note that sectors five and six cannot span more than $\alpha^{\max} = 90° - \alpha^*$, where α^* is defined from (3) by the minimum value of valid NDVI over vegetated areas, taken as equal to 0.1 in this study,

$$0.1 = \frac{\operatorname{tg}(\alpha^*) - 1}{\operatorname{tg}(\alpha^*) + 1} \Rightarrow \alpha^* = 50.71°$$

resulting in $\alpha^{\max} = 39.29°$. Note that sectors four and six will collapse to $0°$ as $NDVI \to 1$.

The question then is, what variations in the leaf area of the canopy and/or the background (soil, litter, understorey, moss or snow) properties produce the observed changes in channel reflectances? To address this question, we use a recently developed radiation model that characterizes radiative transfer in heterogeneous vegetated surfaces using stochastic concepts [39]. To obtain a general picture of changes in the spectral space when the system (vegetation + background) is changing, it is sufficient to consider horizontally homogeneous canopy. For this purpose, leaf optical properties were assumed to be invariant and set as follows (based on average data from a spectral data bank): for grasses, refl$_{\mathrm{red}}$ = 0.070, refl$_{\mathrm{nir}}$ = 0.49; trans$_{\mathrm{red}}$ = 0.030, trans$_{\mathrm{nir}}$ = 0.43; for needle forests, refl$_{\mathrm{red}}$ = 0.055, refl$_{\mathrm{nir}}$ = 0.498; trans$_{\mathrm{red}}$ = 0.040, trans$_{\mathrm{nir}}$ = 0.386. In model calculations we used averaged optical properties of two species due to negligible effect of difference between them on model output. The initial state of the system is a bare background and is specified by background reflectance. The controlling parameter of

the system is leaf area index (LAI). As LAI increases against an invariant background, the system moves along trajectories (soil or background isolines) in the spectral space away from the initial state. To observe different trajectories, we varied initial conditions (background reflectances) according to the background line concept [40]: $\rho_{\mathrm{nir}}^{\mathrm{background}} = 1.2 \cdot (\rho_{\mathrm{red}}^{\mathrm{background}} + 0.04)$, where $\rho_{\mathrm{red}}^{\mathrm{background}}$ and $\rho_{\mathrm{nir}}^{\mathrm{background}}$ are background reflectances at red and near-infrared wavelength. The set of calculated trajectories (soil isolines) is shown in Fig. 14, which also shows LAI isolines, along which LAI is constant, while the background reflectance changes (LAI change between adjacent LAI isolines is 0.25). Note that for very dark backgrounds, increasing leaf area increases both red and near-infrared reflectances, while for backgrounds of intermediate brightness, red reflectance decreases and near-infrared reflectance increases. In the case of very bright backgrounds, increasing leaf area decreases both red and near-infrared reflectances. In the case of dense canopies the trajectories converge to a common point in the spectral space, the reflectance when leaf area tends to infinity. The location of this point is determined mostly by leaf optical properties and also by canopy structural features (leaf normal orientation distribution, geometry, etc.) For example, the location of this limiting point [hemispherical reflectances of canopy, $\mathrm{R}^{\mathrm{canopy}}(\lambda)$] can be analytically evaluated using a two-stream approximation [42] for the case of a horizontally homogeneous canopy with flat horizontal leaves

$$\lim_{\mathrm{LAI} \to \infty} \mathrm{R}^{\mathrm{canopy}}(\lambda) \to \frac{1 - \tau(\lambda) - \sqrt{(1 - \tau(\lambda))^2 - \rho^2(\lambda)}}{\rho(\lambda)}$$

(5)

where $\rho(\lambda)$, $\tau(\lambda)$ are leaf hemispherical reflectance and transmittance at wavelength λ.

The channel reflectance changes shown in Figs. 9 and 10 can be explained with the aid of Fig. 14. In needle forests it is unlikely that LAI can change significantly during a ten-year period. Instead, NDVI change could be due to changes in background reflectance. As shown in Fig. 14, the movement along a LAI isoline from high toward lower background reflectances will result in decrease of red and near-infrared reflectances and increase of NDVI. The decrease in background reflectance can be attributed to progressively declining snow cover extent over the period of satellite record (1982–1994). This feedbacks positively on near surface temperatures and the accompanying warming results in an earlier onset of spring time vegetation growth, perhaps mostly in the understorey.

In the case of grasses, the change in reflectances is more complex—these are two distinct signatures of change. One of these, corresponding to near-infrared reflectance increase, can be attributed to LAI increase, that is, the grasses become more abundant. This agrees well with the pattern shown in Fig. 14, at low background reflectances. The second signature, corresponding to decrease of both red and near-infrared reflectances, a feature that this biome has in common with needle forests, must be also attributed to decline in snow cover extent. From Fig. 9 it appears that this signature while well observed in March and is negligible in April, thus corresponds to progressively declining snow cover in transition from winter to summer. More importantly, the signature of decreased red and near-infrared was observed in data only in cool season for both canopy types. The evidence for both declining snow cover extents and feedback effect on temperature can be found in the literature [25], [36], [37].

The mechanism by which NDVI increases as a result of decrease in background reflectance can be described quantitatively in terms of the sensitivity of NDVI to background reflectance variations. Assume that the hemispherical spectral reflectances of the inert background underneath the trees obeys functional dependencies, for instance, of the linear form [40],

$$\rho_{\text{nir}}^{\text{background}} = \alpha \cdot \rho_{\text{red}}^{\text{background}} + \beta \qquad (6)$$

where $\rho_{\text{red}}^{\text{background}}$ and $\rho_{\text{nir}}^{\text{background}}$ are background reflectances at red and near-infrared wavelength. The existence of a functional dependency is required in order for the derivatives shown below to exist. The sensitivity, or the derivative of NDVI with respect to red or near-infrared background reflectances, it does not matter which, as they are dependent, can be calculated as

$$\frac{\partial NDVI}{\partial \rho_{\text{red}}^{\text{background}}} \Delta \rho_{\text{red}}^{\text{background}}$$
$$= 2 \cdot \frac{(\text{nir}' \cdot \text{red} - \text{nir} \cdot \text{red}')}{(\text{nir} + \text{red})^2} \Delta \rho_{\text{red}}^{\text{background}}. \quad (7)$$

Since the derivatives cannot be evaluated directly from data, (7) can be rewritten in a finite form as

$$\Delta \text{NDVI} = 2 \cdot \frac{\left(\dfrac{\Delta \text{nir}}{\Delta \text{red}} \text{red} - \text{nir}\right)}{(\text{nir} + \text{red})^2} \cdot \text{red}' \cdot \Delta \rho_{\text{red}}^{\text{background}}. \quad (8)$$

The remaining derivative of channel reflectances, red′, in (8) earlier can be calculated from radiative transfer theory, which explicitly parameterizes the influence of background reflectance on the intensity of the radiation field in canopy (see for example [41])

$$\text{I}(\lambda) = \text{I}^{\text{BS}}(\lambda) + \frac{\rho^{\text{background}}(\lambda)}{1 - \rho^{\text{background}}(\lambda) \cdot \text{R}^{\text{S}}(\lambda)} \cdot \text{T}^{\text{BS}}(\lambda) \cdot \text{I}^{\text{S}}(\lambda)$$
$$(9)$$

where $\text{I}(\lambda)$ is the channel reflectance at wavelength λ, $\text{I}^{\text{BS}}(\lambda)$ is the reflectance for the black soil problem $\text{I}^{\text{S}}(\lambda)$ is the reflectance for the soil problem, $\text{T}^{\text{BS}}(\lambda)$ is transmittance for black-soil problem and $\text{R}^{\text{S}}(\lambda)$ is a hemispherical reflectance for the soil problem. The black soil problem describes the radiation regime within a vegetation canopy for the case of a black or completely absorbing surface underneath the medium. The soil problem describes the radiation field in a vegetation canopy generated by anisotropic heterogeneous wavelength-independent sources located at background below the canopy [41]. The derivative of $\text{I}(\lambda)$ with respect to $\rho^{\text{background}}(\lambda)$ is

$$\frac{\partial \text{I}(\lambda)}{\partial \rho^{\text{background}}(\lambda)}$$
$$= \frac{1}{(1 - \rho^{\text{background}}(\lambda) \cdot \text{R}^{\text{S}}(\lambda))^2} \text{T}^{\text{BS}}(\lambda) \cdot \text{I}^{\text{S}}(\lambda).$$

Accounting for (cf. [39] and [41])

$$\text{T}(\lambda) = \frac{\text{T}^{\text{BS}}(\lambda)}{1 - \rho^{\text{background}}(\lambda) \cdot \text{R}^{\text{S}}(\lambda)} \qquad (10)$$

we obtain

$$\frac{\partial \text{I}(\lambda)}{\partial \rho^{\text{background}}(\lambda)} = \text{T}(\lambda) \frac{\text{I}^{\text{S}}(\lambda)}{1 - \rho^{\text{background}}(\lambda) \cdot \text{R}^{\text{S}}(\lambda)} \quad (11)$$

where $\text{T}(\lambda)$ is canopy transmittance. Equations (8) and (11) present exact mathematical expression of the sensitivity of NDVI to variation in background reflectance. The physical meaning of these equations is clear: the lower the optical thickness of the canopy (lower absorbtance and higher transmittance) the higher the influence of background on channel reflectance and NDVI. On the other hand, we require that the background be covered by vegetation (LAI > 0) because we do not consider the limiting case of bare background, such areas are excluded (NDVI > 0.1) from our analysis of vegetation. Also note, that NDVI is insensitive to background reflectance variations even for nonzero transmittance only in one case, when [cf. Equation (8)]

$$\frac{\Delta \text{nir}}{\Delta \text{red}} \text{red} - \text{nir} \equiv 0$$

which results in a linear dependency between channel reflectances of the form nir $= \text{k} \cdot \text{red} + \beta$, which is the NDVI isoline (Fig. 14).

AVHRR channel data do not provide enough information to evaluate the right-hand side of (11). One possible solution is to work with generic values of canopy transmittances and reflectances of needle forests (from recent measurements
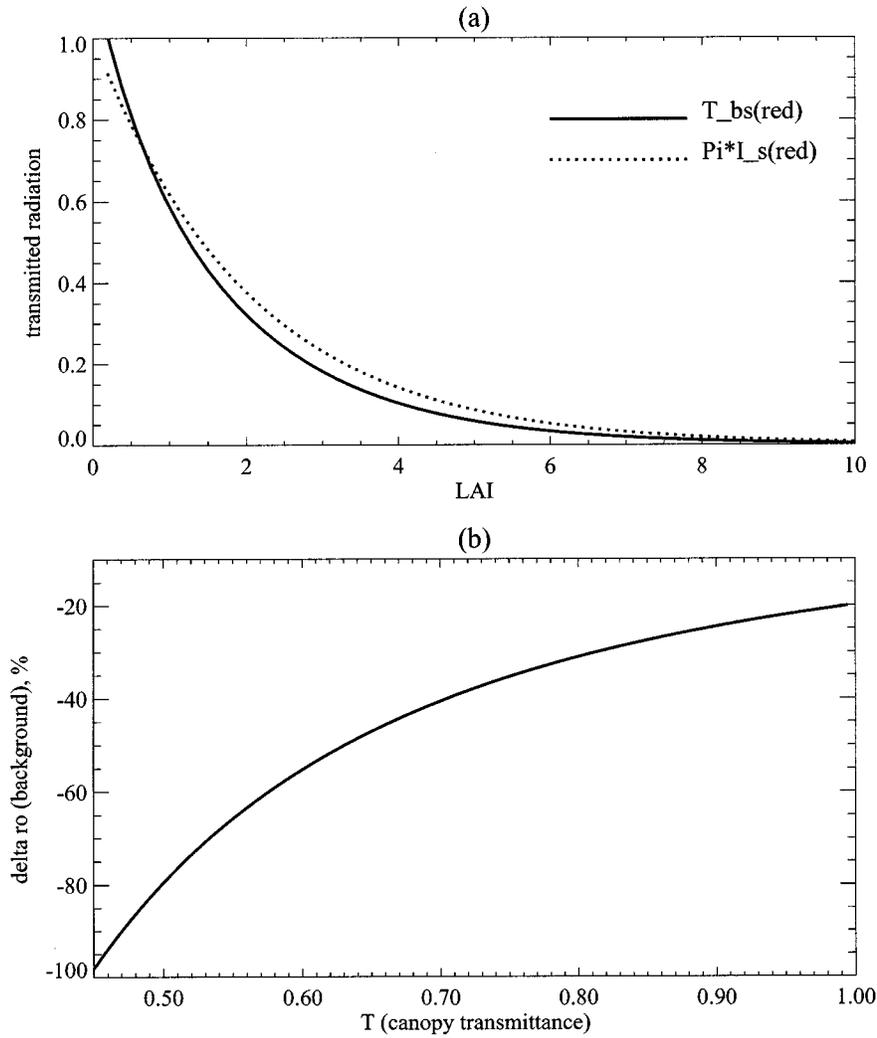
Fig. 15.   Panel (a) shows $\pi \cdot \mathrm{I}^{\mathrm{S}}$ (red) (dotted line) and its approximation by T^{BS} (red) (solid line), cf. Equation (12). The data were generated by a stochastic RT model [39]. The parameters used are: ratio of direct to total solar radiation, 0.5; leaf reflectance and transmittance at red wavelength, $\mathrm{refl}_{\mathrm{red}} = 0.055$, $\mathrm{trans}_{\mathrm{red}} = 0.040$ (this corresponds to the case of needle forests), $\mathrm{SZA} = 23°$. Panel (b) presents upper boundary of background reflectance variations for different values of canopy transmittance, required to explain observed NDVI changes over needle forests.

over coniferous forests, for instance, [43]) and approximate $\mathrm{T}(\lambda)$, $\rho^{\mathrm{background}}(\lambda)$, $\mathrm{R}^{\mathrm{S}}(\lambda)$, $\mathrm{I}^{\mathrm{S}}(\lambda)$. But, we must first address at least two issues: 1) the problem of registration between AVHRR measurements and field data, and 2) the problem of spatial scaling, when point field measurements must be scaled to 8 km AVHRR measurements. In the latter case, dense forest measurements cannot represent averages over large areas, because in general the canopy will be sparser. Thus, the kind of data required was not available to us and we restrict further analysis to obtaining an estimate of variation for the right hand side of (11). Taking into account that [cf. Fig. 15(a)]

$$\pi \cdot \mathrm{I}^{\mathrm{S}}(\lambda) \geq \mathrm{T}^{\mathrm{BS}}(\lambda) \tag{12}$$

and combining it with (8), (10), and (11), we have the following estimation:

$$\Delta \mathrm{NDVI} \geq \frac{2}{\pi} \cdot \mathrm{T}^2(\mathrm{red}) \cdot \frac{\left(\dfrac{\Delta \mathrm{nir}}{\Delta \mathrm{red}} \cdot \mathrm{red} - \mathrm{nir} \right)}{(\mathrm{nir} + \mathrm{red})^2} \cdot \Delta \rho_{\mathrm{red}}^{\mathrm{background}} \tag{13}$$

For the AVHRR channel data over needle forests during, for instance, March (cf. Fig. 8),

$$\frac{\dfrac{\Delta \mathrm{nir}}{\Delta \mathrm{red}} \cdot \mathrm{red} - \mathrm{nir}}{(\mathrm{nir} + \mathrm{red})^2} = -0.5079.$$

Thus, (13) can be rewritten as

$$\Delta \mathrm{NDVI} \geq -\frac{\mathrm{T}^2(\mathrm{red})}{\pi} \cdot \Delta \rho_{\mathrm{red}}^{\mathrm{background}}. \tag{14}$$

In our case $\Delta \mathrm{NDVI} = 0.0633$. The estimate of background reflectance change for different values of canopy transmittance is shown in Fig. 15(b). For cases when $\mathrm{T}^2 \geq 0.5$, background reflectance decrease less then 40% will completely explain observed NDVI change. This is feasible if some bright snow patches of background are replaced by dark soil or vegetation. The analysis can be improved with the availability of large area mean transmittances and reflectances as well as details of geometry and information on seasonal variation of optical properties of vegetation.

V. CONCLUDING REMARKS

The northerly latitudes (23.6°–90° N) have warmed by about 0.8 °C since the early 1970s but not all areas have warmed uniformly [25]. The cool seasons, winter and spring, exhibit pronounced warming, amplified due to the positive feedback associated with the decline in snow cover extent [37]. This warming was hypothesized to have caused progressively earlier onset of spring greening and longer growing seasons in the north, as evidenced in the NDVI data from 1981–1991 [4]. Here, we extend the analysis of Myneni *et al.* with an improved NDVI data set and confirm the northerly greening trend (Fig. 4). Analysis of the channel reflectance data in spring time over Northern Europe and Scandinavia indicates that this NDVI increase results from spectral reflectance changes that are vegetation type dependent. In grasses, the NDVI increase is a result of increase in near-infrared reflectance and a slight decrease in red reflectance (Fig. 9). On the other hand, in needle forests, both red and near-infrared reflectance decrease contribute to the NDVI increase (Fig. 10). These interannual reflectance changes are similar to seasonal changes during the spring period when green leaf area increases and photosynthetic activity ramps up (Fig. 11). Both model calculations and theoretical analysis confirm the hypothesis that warming driven reductions in snow cover extent and earlier onset of greening cause such changes in spectral reflectances over vegetated land areas. Therefore, we conclude that the northerly greening trend observed in the NDVI data is warming driven.

REFERENCES

[1] C. J. Tucker, H. E. Dregne, and W. W. Newcomb, "Expansion and contraction of Sahara desert from 1980 to 1990," *Science*, vol. 253, pp. 299–301, 1991.

[2] W. T. H. Liu, O. Massambani, and C. A. Nobre, "Satellite recorded vegetation response to drought in Brazil," *Int. J. Climatol.*, vol. 14, pp. 343–354, 1994.

[3] L. Di and D. A. Hastings, "Temporal stability of some global NDVI products derived from NOAA/AVHRR GVI," *Int. J. Remote Sensing*, vol. 16, pp. 3569–3583, 1995.

[4] R. B. Myneni, C. D. Keeling, C. J. Tucker, G. Asrar, and R. R. Nemani, "Increased plant growth in the northern high latitudes from 1981 to 1991," *Nature*, vol. 386, pp. 698–702, 1997.

[5] J. Cihlar, J. M. Chen, Z. Li, F. Huang, R. Latifovic, and R. Dixon, "Can interannual land surface signal be discerned in composite AVHRR data?," *J. Geophys. Res.*, vol. 103, no. D18, pp. 23 163–23 172, 1998.

[6] C. M. Malstrom, M. V. Thompson, G. P. Juday, S. Los, J. T. Randerson, and C. B. Field, "Interannual variation in global-scale net primary production: Testing model estimates," *Global Biogeochem. Cycles*, vol. 11, pp. 367–392, 1997.

[7] P. Maisongrande, A. Ruimy, G. Dedieu, and B. Saugier, "Monitoring seasonal and interannual variations of gross primary productivity, net primary productivity and net ecosystem productivity using diagnostic model and remotely sensed data," *Tellus*, vol. 478, pp. 178–190, 1995.

[8] K. Ichii, Y. Matsui, Y. Yamaguchi, and K. Ogawa, "Comparison of global net primary production trends obtained from satellite-based normalized difference vegetation index and carbon cycle model," *Global Biogeochem. Cycles*, vol. 15, no. 2, pp. 351–363, 2001.

[9] M. E. James and S. N. V. Kalluri, "The Pathfinder AVHRR land data set: An improved coarse-resolution data set for terrestrial monitoring," *Int. J. Remote Sensing*, vol. 15, pp. 3347–3364, 1994.

[10] C. J. Tucker, "History of the use of AVHRR data for land applications," in *Advances in the Use of NOAA AVHRR Data for Land Application*, G. D'Souza, Ed. Dodrecht, The Netherlands: Kluwer, 1996, pp. 1–19.

[11] R. B. Myneni, S. O. Los, and C. J. Tucker, "Satellite-based identification of linked vegetation index and sea surface temperature anomaly areas from 1982–1990 for Africa, Australia and South America," *Geophys. Res. Lett.*, vol. 23, pp. 729–732, 1996.

[12] R. B. Myneni, C. J. Tucker, G. Asrar, and C. D. Keeling, "Interannual variations in satellite-sensed vegetation index data from 1981 to 1991," *J. Geophys. Res.*, vol. 103, pp. 6145–6160, 1998.

[13] C. D. Keeling, J. F. S. Chin, and T. P. Whorf, "Increased activity of northern vegetation inferred from atmospheric measurements," *Nature*, vol. 382, pp. 146–149, 1996.

[14] E. F. Vermote and Y. J. Kaufman, "Absolute calibration of AVHRR visible and near infrared channels using ocean and cloud views," *Int. J. Remote Sensing*, vol. 16, pp. 2317–2340, 1995.

[15] S. O. Los, "Calibration adjustment to the NOAA AVHRR normalized difference vegetation index without recourse to component channel 1 and 2 data," *Int. J. Remote Sensing*, vol. 14, pp. 1907–1917, 1993.

[16] S. O. Los, C. O. Justice, and C. J. Tucker, "A global 1 × 1 degree NDVI data set for climate studies derived from the GIMMS continental NDVI data," *Int. J. Remote Sensing*, vol. 15, pp. 3493–3518, 1994.

[17] B. N. Holben, "Characteristics of maximum value composite images for temporal AVHRR data," *Int. J. Remote Sensing*, vol. 7, pp. 1417–1437, 1986.

[18] E. F. Vermote, N. Z. El Saleous, Y. J. Kaufman, and E. Dutton, "Stratospheric aerosol perturbing effect on the remote sensing of vegetation: Correction method for the composite NDVI after the Pinatubo eruption," *Remote Sens. Rev.*, vol. 15, pp. 7–21, 1997.

[19] M. D. Schwartz, "Green-wave phenology," *Nature*, vol. 394, pp. 839–840, 1998.

[20] A. Menzel and P. Fabian, "Growing season extended in Europe," *Nature*, vol. 397, p. 659, 1999.

[21] N. L. Bradley, A. C. Leopold, J. Ross, and W. Huffaker, "Phenological changes reflect climate change in Wisconsin," in *Proc. Natl. Acad. Sci.*, vol. 96, 1999, pp. 9701–9704.

[22] J. T. Randerson, C. B. Field, I. Y. Fung, and P. P. Tans, "Increases in early season ecosystem uptake explain recent changes in the seasonal cycle of atmospheric CO_2 at high northern latitudes," *Geophys. Res. Lett.*, vol. 26, pp. 2765–2769, 1999.

[23] G. Gutman, "On the use of long-term global data of land reflectances and vegetation indices derived from the advanced very high resolution radiometer," *J. Geophys. Res*, vol. 104, pp. 6241–6255, 1999.

[24] R. K. Kaufmann, L. Zhou, Y. Knyazikhin, N. V. Shabanov, R. B. Myneni, and C. J. Tucker, "Effect of orbital drift and sensor changes on the time series of AVHRR vegetation index data," *IEEE Trans. Geosci. Remote Sensing*, vol. 38, pp. 2584–2597, Nov. 2000.

[25] J. Hansen, R. Ruedy, J. Glascoe, and M. Sato, "GISS analysis of surface temperature change," *J. Geophys. Res.*, vol. 104, pp. 30 997–31 022, 1999.

[26] R. B. Myneni, R. Nemani, and S. W. Running, "Estimation of global leaf area index and absorbed par using radiative transfer models," *IEEE Trans. Geosci. Remote Sensing*, vol. 35, pp. 1380–1393, Nov. 1997.

[27] A. Lotsch, Y. Tian, M. A. Friedl, and R. B. Myneni, "Land cover mapping in support of LAI/FPAR retrievals from EOS-MODIS and MISR: Classification methods and sensitivities to errors," Int. J. Remote Sensing, submitted for publication.

[28] C. J. Tucker, J. R. G. Townshed, and T. E. Goff, "African land-cover classification using satellite data," *Science*, vol. 227, pp. 369–375, 1985.

[29] C. J. Tucker, I. Y. Fung, C. D. Keeling, and R. H. Gammon, "Relationship between atmospheric CO_2 variations and satellite-derived vegetation index," *Nature*, vol. 319, pp. 195–199, 1986.

[30] G. Asrar, M. Fichs, E. T. Kanemasu, and J. L. Hatfield, "Estimating absorbed photosynthetic radiation and leaf area index from spectral reflectance in wheat," *Agron. J.*, vol. 76, pp. 300–306, 1984.

[31] I. Y. Fung, C. J. Tucker, and K. C. Prentice, "Application of advanced very high resolution radiometer vegetation index to study atmosphere–biosphere exchange of CO_2," *J. Geophys. Res.*, vol. 92, pp. 2999–3015, 1987.

[32] R. B. Myneni, F. G. Hall, P. J. Sellers, and A. L. Marshak, "The interpretation of spectral vegetation indexes," *IEEE Trans. Geosci. Remote Sensing*, vol. 33, pp. 481–486, June 1995.

[33] Y. J. Kaufmann, "The atmospheric effect on remote sensing and its correction," in *Theory and Applications of Optical Remote Sensing*, G. Asrar, Ed. New York: Wiley, 1989, pp. 336–429.

[34] M. D. Dettinger, M. Ghil, C. M. Strong, W. Weibel, and P. Yiou, "Software for singular spectrum analysis of noisy timeseries," *EOS, Trans. Amer. Geophys. Union*, vol. 76, no. 2, p. 12, 1995.

[35] R. Vautard, P. Yiou, and M. Ghil, "Singular-spectrum analysis: A toolkit for short, noisy chaotic signals," *Physica D*, pp. 95–126, 1992.

[36] W. L. Chapman and J. E. Walsh, "Recent variations of sea ice and air temperature in high latitudes," *Bull. Amer. Meteorol. Soc.*, vol. 74, pp. 33–47, 1993.

[37] P. Y. Groisman, T. R. Karl, and R. W. Knight, "Observed impact of snow cover on heat balance and the rise of continental spring temperatures," *Science*, vol. 263, pp. 198–200, 1994.

[38] D. S. Broomhead and G. P. King, "Extracting qualitative dynamics from experimental data," *Phys. D*, vol. 20, pp. 217–236, 1986.

[39] N. V. Shabanov, Y. Knyazikhin, F. Baret, and R. B. Myneni, "Stochastic modeling of radiation regime in discontinous vegetation canopies," *Remote Sens. Environ.*, vol. 74, no. 1, pp. 125–144, 2000.

[40] F. Baret, S. Jacquemoud, and J. F. Hanocq, "The soil line concept in remote sensing," *Remote Sens. Rev.*, vol. 7, pp. 65–82, 1993.

[41] Y. Knyazikhin, J. V. Martonchik, R. B. Myneni, D. J. Diner, and S. W. Running, "Synergistic algorithm for estimating vegetation canopy leaf area index and fraction of absorbed photosynthetically active radiation from MODIS and MISR data," *J. Geophys. Res.*, vol. 103, no. D24, pp. 32 257–32 277, 1998.

[42] J. Ross, *The Radiation Regime and Architecture of Plant Stands*. The Hague, The Netherlands: Dr. W. Junk, 1981, pp. 258–260.

[43] O. Panferov, Y. Knjazikhin, R. B. Myneni, J. Szarzhinski, S. Engwald, K. Schitzler, and G. Gravenhorst, "The role of canopy structure in spectral variation of transmission and absorption of solar radiation in vegetation canopies," *IEEE Trans. Geosci. Remote Sensing*, vol. 39, pp. 241–253, Mar. 2001.

Nikolay V. Shabanov was born in Novocherkassk, Russia, on December 2, 1972. He received the M.A. degree in physics from Moscow State University, Russia, in 1996, and the Ph.D. degree in remote sensing from Boston University, Boston, MA, in 2001.

His research interests are in stochastic theory of radiative transfer in vegetation canopies and analysis of satellite vegetation data.

Liming Zhou received the B.S. and M.S. degrees in meteorology from the Nanjing Institute of Meteorology, Nanjing, China, in 1991 and 1994, respectively. He is currently pursuing the Ph.D. degree in the Department of Geography, Boston University, Boston, MA, where he is working on the relation between interannual variability in climate change and global vegetation dynamics observed from satellite sensed dataset.

Dr. Zhou is a recipient of the NASA Earth System Science Graduate Fellowship.

Yuri Knyazikhin received the M.S. degree in applied mathematics from Tartu University, Estonia, and the Ph.D. degree in numerical analysis from the N.I. Muskhelishvilli Institute of Computing Mathematics, the Georgian Academy of Sciences, Tbilisi, GA, in 1978 and 1985, respectively.

He was a Research Scientist at the Institute of Astrophysics and Atmospheric Physics and Tartu University, Computer Center of the Siberian Branch of the Russian Academy of Sciences, from 1978 to 1990. He was an Alexander von Humboldt Fellow from 1992 to 1993, and worked at the University of Göttingen, Germany, from 1990 to 1996. He is currently a Research Associate Professor in the Department of Geography, Boston University, MA. He has worked and published in areas of numerical integral and differential equations, theory of radiation transfer in atmospheres and plant canopies, remote sensing of the atmosphere and plant canopies, ground-based radiation measurements, forest ecosystem dynamics and modeling sustainable multifunctional forest management.

Ranga B. Myneni received the Ph.D. degree in biology from the University of Antwerp, Antwerp, Belgium, in 1985.

Since then, he has been with Kansas State University, Manhattan, the University of Göttingen, Göttingen, Germany, and NASA Goddard Space Flight Center, Greenbelt, MD. He is now a Member of Faculty, Department of Geography, Boston University, Boston, MA. His research interests are in radiative transfer, remote sensing of vegetation, and climate-vegetation dynamics.

Dr. Myneni is a MODIS and MISR science team member.

Compton J. Tucker received the B.S. degree in biology and the M.S. and Ph.D. degrees in forestry from Colorado State University, Fort Collins, in 1969, 1973, and 1975, respectively.

He has been with NASA Space Flight Center, Greenbelt, MD, for over 20 years, planning and conducting research on deforestation and the Earth's climate and biogeochemical cycles.